Sectional Analysis of Engineered Cementitious Composite Beams

Accepted manuscript doi:
10.1680/jmacr.17.00199

Accepted manuscript doi:
10.1680/jmacr.17.00199

Submitted: 24 April 2017

Published online in 'accepted manuscript' format: 12 December 2017

Manuscript title: Sectional Analysis of Engineered Cementitious Composite Beams

Authors: Benny Suryanto, Robin Reynaud and Blair Cockburn

Affiliation: School of Energy, Geoscience, Infrastructure and Society, Institute for Infrastructure and Environment, Heriot-Watt University, Edinburgh, UK

Corresponding author: Benny Suryanto, School of Energy, Geoscience, Infrastructure and Society, Institute for Infrastructure and Environment, Heriot-Watt University, Edinburgh, UK. Tel.: +44-131-451-3817; Fax: +44-131-451-4617.

E-mail: b.suryanto@hw.ac.uk

Accepted manuscript doi:
10.1680/jmacr.17.00199

Abstract

A procedure to predict the flexural response of an Engineered Cementitious Composite (ECC) prismatic beam specimen subjected to four-point bending and its implementation into an Excel spreadsheet are described. It utilises the layered sectional analysis approach and nonlinear ECC constitutive models, allowing for the calculation of the moment-curvature relationship for any selected section of the beam specimen at various stages of loading. Further, the curvature-area method is employed to integrate the sectional response and determine the overall beam deflection profile. To this end, predictions by the proposed method are compared against three series of experiments available in the literature, to provide a better understanding of the relation between the tensile properties of ECC and the corresponding flexural response. It is shown that due to flexural cracking, the beam curvature over the shear span varies nonlinearly from the support and is found to influence the prediction of beam deflection. A series of empirical equations are presented to allow for the quick calculation of tensile strain capacity and tensile strength of ECC based upon flexural test data.

Keywords: Cementitious materials; Fibre-reinforcement; Tensile properties; Quality control

Accepted manuscript doi:
10.1680/jmacr.17.00199

1. Introduction

An Engineered Cementitious Composite (ECC) is a fibre reinforced cement-based composite which, when subjected to tension, exhibits ductile strain-hardening and a high tensile strain capacity, typically in excess of 1% (Li, 2008). This unique response is attributed to the ability of the material to form closely-spaced fine cracks, typically less than 0.1 mm in width and independent of the member size (Li and Stang, 2004). This is in contrast with the post-cracking response of ordinary concrete, which when subjected to the same level of deformation, will exhibit macro cracking thereby requiring additional measures to control crack width. The enhancement in tensile performance may offer an economic solution in situations where cracking and long-term durability are critical (Mechtcherine, 2012; Sisomphon *et al.*, 2013). However, Kanda and co-workers (2006) noted that the implementation of a simple method as part of routine quality testing is central to delivering the anticipated tensile performance of ECC.

Existing methods for ascertaining the tensile properties of ECC are typically performed through direct application of a tensile force at both ends of a test sample, popularly known as the direct/uniaxial tensile test. Dog-bone samples are the most commonly used sample shape as implemented by Kanda *et al.* (2003), Matsumoto *et al.* (2010), Jun *et al.* (2010), Huang *et al.* (2013), van Zijl *et al.* (2015), Suryanto *et al.* (2016) and Kobayashi *et al.* (2016), although prismatic and cylinder samples have also been used, such as by Fukuyama and Suwada (2003), Wang and Li (2007), Yun *et al.* (2007) and Zhou *et al.* (2010). While direct tensile tests provide results which are easy to analyse, the experimental procedure is often difficult to execute to an appropriate standard. Also, the quality of test samples must be very high due to the sensitive nature of the test; in most cases, the level of quality required may not be easily achieved in normal construction practice. The difficulty in testing samples using the direct

Accepted manuscript doi:
10.1680/jmacr.17.00199

tensile method may, therefore, put off some potential users and limit the benefits offered by this novel composite. To promote a more widespread use of ECC, an alternative method which is technically easy to perform must be developed.

The four-point bending test is one of such developments. This test method was adopted initially by Maalej and Li (1994) who introduced the relationship between the flexural strength and tensile strength of an early version of ECC. In this early work, the beam deflection was estimated based on the assumption of constant curvature profile. Kanakubo (2006) proposed the use of crack-opening displacement gauges to directly measure the longitudinal strains over the centre span of a beam specimen, allowing for the actual beam curvature to be obtained and hence the moment-curvature relation. Using this information, the tensile properties were then determined through intermediate calculations. This was a significant step to providing a simple method for regular quality control, which later formed the basis of JCI-S-003-2007 (JCI, 2007). Whilst the proposed test procedure is relatively simple, the extra test requirements such as the need for using special gauges and gluing a number fixing blocks for attaching the gauges prior to testing could prolong preparation and thus may limit its effectiveness for regular and frequent quality control testing.

Qian and Li (2007) sought to simplify the process through the development of *master curves* based upon flexural test results. The curves were obtained by plotting the tensile strain capacity of a wide range of ECC mixes against beam deflection. When deriving the curves, it was assumed that the curvature profile along the shear span is linear and proportional to the point-load deflection, which was an improvement to the assumption made earlier by Maalej and Li (1994). It was shown that the derived curves can also be used to determine the tensile strain capacity of ECC specimens, provided that the test is conducted on a specimen with the same geometry and using the same test set-up. To determine the corresponding tensile

Accepted manuscript doi:
10.1680/jmacr.17.00199

strength, Qian and Li (2008) further extended the work, albeit using a simplified material model, and developed a relationship between the modulus of rupture (MOR) to tensile cracking stress ratio and tensile strain capacity, allowing the tensile strain capacity and tensile strength to be calculated based upon readings from a testing machine without the use of additional test apparatus. A similar approach will be used in the work presented herein, although it will consider the actual curvature profile based on the simple beam theory.

To provide an alternative to the previous development, Soranakom and Mobasher (2008) derived a closed-form solution which can be utilised to characterise the flexural response of fibre reinforced concrete in general, including ECC. It was demonstrated that the prediction for ECC shows a better agreement than that for ordinary fibre reinforced concrete, provided that ECC exhibiting strain-hardening response and hence less pronounced size effect. Another closed-form solution was offered by Hou *et al.* (2012) who proposed the concept of equivalent deflection for varying depths of specimens and presented a method, adapted from ASTM C1609 (ASTM, 2012) and JCI-SF4 (JCI, 1984), to evaluate the toughness capacity of an ultra-high toughness cementitious composite. Further development in the field was made by Shin *et al.* (2015), who adopted the layered section method to predict the flexural response of strain-hardening cement composite with material inhomogeneity present, which thereby experienced localised crack formation prior to the peak load.

In this paper, a simple sectional analysis procedure (hereafter referred to as the Flexural Analysis Tool, or FAsT) is used to predict the flexural response of ECC beam specimens under four-point bending. This analysis procedure will be initially validated by performing three series of analysis on selected test data available in the literature. It will then be employed to perform a parametric study of varying compressive/tensile strengths and tensile strain capacities from which a simple framework for ascertaining the tensile properties of

Accepted manuscript doi:
10.1680/jmacr.17.00199

ECC will be developed. It should be noted that the four-point bending test should not be used to replace the uniaxial tensile test, but rather to accompany it. With the aid of the developed framework, four-point bending tests, as recently employed by Alyousif *et al.* (2016) and Siad *et al.* (2016), can be performed for day-to-day quality control testing with tensile tests validating these results periodically (e.g. to confirm the strain-hardening property, as per JCI-DFRCC Committee (2003)).

2. Research Significance

This work seeks to develop an alternative technique, providing the construction industry with a simple calculation procedure to characterise the tensile properties of ECC. A series of empirical equations are proposed to provide quick calculation of the tensile properties of ECC based on four-point bending test data, which could find use in quality control testing.

3. Overview of the Computational Platform

3.1. Structural Model and Constitutive Relations

Figures 1(a) and (b) present the structural model employed in FAsT, with only half of the beam being modelled due to symmetry. This half-beam length is divided into 11 segments (or, accordingly, 12 cross-sections), with each individual section further subdivided into fine layers having the same width *b* and depth *d* (see Figure 1(c)). The cross-sections are assumed to remain plane after bending and normal to the longitudinal axis. The longitudinal strain in each layer ε_i is determined from the tensile strain at the centroid of the utmost bottom layer $\varepsilon_{t,b}$ using

$$\varepsilon_i = \frac{(y_i - x_c)}{(h - x_c - 0.5d)} \gamma \varepsilon_{t,b} \quad (1)$$

where y_i and x_c are the positions of the centroid of layer i and the neutral axis, respectively, both relative to the top of the beam (mm); h is the overall depth of the beam (mm); n is the number of layer; and γ is a scaled factor. Failure is assumed to take place when the strain at the centroid of the utmost bottom layer (viz, $i = n$) over the centre span reaches the tensile strain capacity of the ECC, $\varepsilon_{t,b} = \varepsilon_{t,u}$, and γ = 1.0.

The longitudinal stresses acting on each layer are determined from the corresponding longitudinal strains using the constitutive relations presented in Figure 2, which are based on the work by Suryanto *et al.* (2010b and 2010c). The curve describing the response in compression is adapted from the elasto-plastic fracture model for concrete proposed earlier by Maekawa *et al.* (2003):

$$f_c = \omega_c K_o E_o \left(\varepsilon_i - \varepsilon_p\right) \tag{2}$$

where the fracture parameter, K_o; the initial stiffness, E_o, (MPa); and the plastic strain, ε_p, defined as

$$K_o = exp\left[-0.73\frac{\varepsilon_i}{\varepsilon_c'}\left[1 - exp\left(-1.25\frac{\varepsilon_i}{\varepsilon_c'}\right)\right]\right] \tag{2a}$$

$$E_o = 2\frac{f_c'}{\varepsilon_c'} \tag{2b}$$

$$\varepsilon_p = \beta\left[\frac{\varepsilon_i}{\varepsilon_c'} - \frac{20}{7}\left[1 - exp\left(-0.35\frac{\varepsilon_i}{\varepsilon_c'}\right)\right]\right]\varepsilon_c' \tag{2c}$$

where f_c' is the ECC compressive strength (MPa), ε_c' is the strain at the peak compressive strength and β is the strain-rate factor (taken as 1.0). The compressive strength reduction factor due to transverse cracking, ω_c, is taken as 1.0. The base response in tension is assumed to be in a bilinear shape (hereafter referred to as the BL model), with the first linear part describing the elastic response of the ECC and the second part describing the strain-hardening response, as given by

$$f_t = \begin{cases} \omega_t E_e \varepsilon_i & \text{if} \quad 0 < \varepsilon_i < \varepsilon_{t,cr} \\ \omega_t \left[E_{sh} \left(\varepsilon_i - \varepsilon_{t,cr} \right) + f_{t,cr} \right] & \text{if } \varepsilon_{t,cr} < \varepsilon_i < \varepsilon_{t,u} \end{cases} \quad (3)$$

where E_e is the elastic modulus (MPa); E_{sh} is the stiffness during the strain-hardening stage (MPa); $\varepsilon_{t,cr} = \frac{f_{t,cr}}{E_e}$; $f_{t,cr}$ is the tensile cracking stress and equal to $\alpha f_{t,u}$ (MPa), with α being the ratio of tensile cracking stress to tensile strength; and ω_t is the tensile strength reduction factor due to transverse cracking (taken as 1.0). In the present work, the ECC is also modelled, for comparative purposes, as an elastic-plastic (EP) material as this model (or perfectly plastic model) has been frequently used due to its simplicity (Kanakubo, 2006; Qian and Li, 2008; Suryanto *et al.*, 2010a; Suryanto et al., 2016). In this model, $\varepsilon_{t,cr}$ is taken as $\frac{f_{t,u}}{E_e}$ and α is taken as 1.0 (E_{sh} = 0).

Once the stresses have been computed, the longitudinal force in each layer is then computed as the product of the stress and the area of each layer (see the summary of the calculation procedure in Figure 3). These forces are then added up to determine whether or not the section is in equilibrium. If not, the position of the neutral axis x_c is adjusted in the next step of iteration. The same equilibrium check is also carried out on the internal moment against the externally applied moment, with the tensile strain at the centroid of the utmost bottom layer $\varepsilon_{t,b}$ being adjusted iteratively. This iterative process continues until convergence is achieved to an acceptable level of error. This iteration is done automatically using the Do-loop and Goal Seek functions via the Visual Basic for Application (VBA) editor.

3.2. Computer Implementation

The developments presented in Section 3.1 were implemented in an Excel spreadsheet to make it readily available to other researchers and practitioners in general. Figure 4(a) presents the structure of FAsT, which in general comprises one master worksheet (Worksheet 1),

Accepted manuscript doi:
10.1680/jmacr.17.00199

where a user can populate the input data and view the analysis results (see Figures 4(b) and (c)), and other worksheets responsible for computing detailed flexural response at prescribed displacement increments. By default, FAsT considers two tensile stress-strain models: elastic plastic (EP) and bilinear (BL) models, and nine displacement increments, which are determined from the tensile strain at the centroid of the utmost bottom layer of a critical section over the central span. These increments were determined using the scaled factor, γ (see Equation 1) which was defined as 1%, 2.5% 5%, 10%, 15%, 25%, 50%, 75% and 100% of the tensile strain capacity of the ECC, $\varepsilon_{t,u}$. Accordingly, there are eighteen worksheets responsible for performing calculations based on the two tensile models considered (nine per tensile model).

To run a simulation, a user will need to populate the form provided in the first worksheet under the 'Geometry Information' and 'Material Properties' headers, as shown in Figure 4(b). The required input data includes: the width *b*, overall depth *h*, shear span *a*, overall span *L*, ratio of cracking strength to the ultimate tensile strength α, ultimate tensile strength $f_{t,u}$, tensile strain capacity $\varepsilon_{t,u}$, modulus of elasticity E_e, compressive strength f_c', and strain at the compressive strength ε_c'. The simulation can then be performed by simply clicking the 'RUN' button. The time required to run an analysis depends upon the number of layers employed in the beam cross-section; when very fine (i.e., 100) layers are used, it takes less than 5 minutes with an Intel® CoreTM i5-4200U 2.3GHz laptop with 4GB memory. Analysis results will be then provided in the right-hand-side of the first worksheet; an example is presented in Figure 4(c) based on the work by Paegle *et al.* (2016). The upper left plots show the member geometry and locations of support and loading points, with plots of the input material properties presented directly below. The upper central plots display the predicted curvature and deflection profiles based on the tensile properties specified by the user (viz, in the form

Accepted manuscript doi:
10.1680/jmacr.17.00199

of a bilinear (BL) stress-strain relation); for comparative purposes, the upper right plots display the corresponding profiles based on the elastic-plastic (EP) tensile model. The lower left plots compare the predicted longitudinal stresses over the depth of a beam based on the two tensile (BL and EP) models, with the corresponding load-deflection responses plotted in the lower central plots. Finally, the plots on the lower right show the predicted moment-curvature responses produced by the two tensile models.

4. Analysis Results and Discussion

Three series of analysis were performed to demonstrate the validity of the present developments. The first series of analysis was carried out on ECC beam specimens, 76.2×101.6 mm^2 in cross-section, tested under two-point loading conditions over three equal spans (101.6 mm each), as per Maalej and Li (1994). The ECC was reinforced with polyethylene fibres at a volume fraction of 2%. The following material data were assumed in the analysis: E_s = 14 GPa; α = 0.63 (BL model) and 1.0 (EP model); $f_{t,u}$ = 4.6 MPa; $\varepsilon_{t,u}$ = 5.6 %; f_c' = 60 MPa; and ε_c' = 1 %. Figure 5(a) presents the two tensile models assumed in the analysis along with the envelope of the tensile stress-strain response obtained from a coupon test.

The predicted and observed equivalent flexural stress versus midpoint deflection responses are presented in Figure 5(b), together with the predictions by Maalej and Li (1994) and Soranakom and Mobasher (2008) for comparative purposes. The equivalent flexural stress, f_{eq} (MPa), is calculated based on the assumption that the material remains elastic:

$$f_{eq} = \frac{6M}{bh^2} \tag{4}$$

where $M = 0.5Pa$; P is the applied load (N); a is the shear span (mm); b and h are, respectively, the width and depth of test specimen (mm) (see Fig. 1(a)). It is evident that the

Accepted manuscript doi:
10.1680/jmacr.17.00199

predicted response using the bilinear (BL) model follows closely that reported by Soranakom and Mobasher (2008) and agrees well with one of the experimental data. However, it tends to underestimate the load and deflection capacity of the other two data sets, with the disparity expected due to possible variations in the tensile properties of the ECC. It is also evident that the predicted response is stiffer than that reported by Maalej and Li (1994) which can be associated with the assumption of a constant curvature profile along the beam length, resulting in a larger area under the curvature profile and hence the larger deflection prediction. It is also evident from Figure 5(b) that the assumed tensile stress-strain profile has a significant influence on the post-cracking response (the nonlinear part of the curves). The EP model exhibits a much sharper post-cracking response, followed by a flat-top response with increasing deflection until failure, whereas the BL model exhibits a more gradual increase in stress until failure, resembling more closely the behaviour recorded experimentally. This is due to the assumption made in the EP model: considering the stress at first cracking, $f_{t,cr}$, equals to that at ultimate state, $f_{t,u}$.

It is interesting to note from Figure 5(b) that the assumed tensile stress-strain response has an influence on the predicted deflection capacity, with the EP model giving a more conservative estimate. To explain this feature, the predicted curvature profiles along the beam are shown in Figures 5(c) and (d). It is evident that the curvature over the shear span varies linearly from the support as long as the beam remains in the elastic range (see the inset in Figure 5(d) obtained immediately after cracking (Steps 1–3)). When the beam over the centre span begins to crack, a nonlinear curvature profile within the shear span is produced, with the curvature over the centre span remaining constant. The start of the nonlinear part of the curvature profile indicates the location of transition point from elastic to cracked state, which moves outward from the load-point toward the support as the load increases. From these two

Accepted manuscript doi:
10.1680/jmacr.17.00199

curvature profiles, it is apparent that the EP model produces a slightly larger value of curvature over the constant moment span and a more drastic curvature profile as it reaches the centre span than the BL model. This latter is due to the assumed value of $f_{t,cr}$ which, in the EP model, is taken equal to $f_{t,u}$ thereby making sections away from the maximum moment span increasingly resistant to cracking. Accordingly, the cracks in the EP model form closer to the centre region. Although the predicted curvature based on the EP model is higher at the centre span, the overall area under the curvature profile obtained using the BL model is larger which explains the larger deflection exhibited by the BL model.

To further demonstrate the validity of the framework, the spreadsheet was employed to simulate the response of ECC beam specimens tested by Kanakubo (2006). The ECC beams were 100×100 mm^2 in cross-section and tested under two-point loading condition over three equal 100 mm span. The ECC was reinforced with polyvinyl alcohol (PVA) fibres at a volume fraction of 2%. The material data employed in the analysis were assumed as: E_s = 19 GPa; α = 0.7 (BL model) and 1.0 (EP model); $f_{t,u}$ = 4 MPa; $\varepsilon_{t,u}$ = 2.4 %; f_c' = 31.3 MPa; and ε_c' = 0.55%. The tensile models employed in the analysis along with the results of direct tensile tests are presented in Figure 6(a). The tensile test data were obtained from two dog-bone samples with cross-sections of 100×60 (thick) mm over their central regions.

Figure 6(b) presents the predicted and observed moment-curvature response of the beams at one of the critical sections over the centre span, with the points representing the envelope of the test data and the lines representing the predicted response. Additionally, the corresponding flexural stress-deflection responses are presented in Figure 6(d). It is evident from these two figures that the BL model is in better agreement with the test data and the EP model overestimates the flexural strength by approximately 11%. This is due to the

Accepted manuscript doi:
10.1680/jmacr.17.00199

overestimation of tensile stress under the neutral axis (see Figure 6(c)) highlighting the importance of using appropriate tensile model when determining flexural strength.

To further validate the proposed method, another series of analysis was carried out to simulate the series of ECC beam specimens tested recently by Paegle *et al.* (2016). The test setup was adapted from ASTM C1609 (ASTM, 2012), with the specimens subjected to third point loading over an individual span of 150 mm. The width of the beams, *b*, was kept constant at 150 mm, whereas the depth, *h*, was varied: 50 mm, 75 mm and 150 mm, producing a shear span-to-depth ratio of 0.33, 0.5, and 1.0, respectively. The ECC was reinforced with 8 mm long PVA fibres at a volume fraction of 2%. The material data used in the analysis were assumed as: E_s = 18 GPa; α = 0.8 (BL model) and 1.0 (EP model); $f_{t,u}$ = 4.1 MPa; $\varepsilon_{t,u}$ = 2.2 %; f_c' = 47.5 MPa; and ε_c' = 0.5%. The tensile models employed in the analysis are presented in Figure 7(a), together with the envelope of tensile stress-strain data obtained from dog-bone specimens, which had cross sections of 50×22 (thick) mm^2 over their central regions.

Comparison of predicted and observed flexural responses of the beams is presented in Figures 7(b) to (d) for the three different beam depths. It is apparent from these Figures that the predictions employing the BL model, once again, are in better agreement with the observed response. It is evident that as the beam thickness increases, the predicted load carrying capacity increases whereas the predicted flexural strength remains virtually constant. It is also evident that the predicted responses for beams with reduced thicknesses (50 mm and 75 mm) are in a better agreement with the test data than those for 150 mm thick beam specimens. The disparity in the latter can be attributed to the effect of shear as reported by Paegle *et. al* (2016) and due to possible differences in fibre orientation between the dog-bone and the prismatic specimens resulting from the thickness difference (Kanakubo, 2007).

Accepted manuscript doi:
10.1680/jmacr.17.00199

5. Calculation of Tensile Properties using a Simplified Approach

In this section, FAsT is used to carry out sensitivity analysis, with the aim of developing a simple method that can be implemented in routine quality testing for ascertaining the tensile properties of ECC.

5.1 Predictions based on empirical equations

A sensitivity analysis was carried out on the setup proposed by Paegle *et. al* (2016) for specimens with reduced thicknesses (50 and 75 mm), as recommended in the paper. The material parameters used in the analysis were: E_s = 18 GPa; α = 0.8 (BL model); f_c' = 40, 50 and 60 MPa; $f_{t,u}$ = 3.5, 4 and 5 MPa; $\varepsilon_{t,u}$ = 0.4 – 4%; and ε_c' = 0.5%. The specimen width, *b*, was set constant at 150 mm.

Figure 8(a) presents the predicted mid- and load-point beam deflections corresponding to the peak load capacity plotted against tensile strain capacity, with the four discrete tensile strain values highlighted with data marker and connected using dashed line for clarity. Similar to the observations by Qian and Li (2006), it is evident that the two parameters are proportionally correlated; all values lie on a narrow band of straight lines, with the width of the band increasing with increasing tensile strain capacity and with the slope of the lines increasing with increasing beam thickness. The generic relationship relating the two parameters is given by:

$$\varepsilon_{t,u} = \begin{cases} 0.28\delta_{u,m} - 0.1 \\ 0.33\delta_{u,l} - 0.1 \end{cases} \quad \text{if } h = 50 \text{ mm} \tag{5a}$$

$$\varepsilon_{t,u} = \begin{cases} 0.41\delta_{u,m} - 0.1 \\ 0.50\delta_{u,l} - 0.1 \end{cases} \quad \text{if } h = 75 \text{ mm} \tag{5b}$$

Accepted manuscript doi:
10.1680/jmacr.17.00199

where $\delta_{u,m}$ is the mid-point deflection at the peak strength (mm) and $\delta_{u,l}$ is the corresponding load-point deflection (mm); this equation gives $\varepsilon_{t,u}$ in %. During a quality control check, one can determine either load- or mid-point deflection experimentally and then either use Figure 8(a) or Equation 5(a) or (b) to estimate tensile strain capacity. However, it should be noted that while load-point deflection is easy to measure, as it only requires readings from a testing machine, appropriate measures should be taken to avoid additional deflection resulting from bedding error and rig deformation being recorded, thereby resulting in false readings.

To determine the corresponding tensile strength, the relationship between the equivalent elastic flexural strength (MOR) to tensile strength ($f_{t,u}$) ratio and tensile strain capacity is presented in Figure 8(b), with the strain values varied between $\varepsilon_{t,cr}$ and 4%. It is apparent that the stress ratio increases rapidly with increasing tensile strain capacity until it reaches approximately 0.4% and the increase thereafter becomes less significant. It is interesting to note that unlike the relation between tensile strain capacity and beam deflection capacity shown earlier in Figure 8(a), the stress ratio is not dependent on beam thickness and the location of deflection measurement. The stress ratio for tensile strain capacity greater than 0.4% can be approximated from:

$$\frac{MOR}{f_{t,u}} = 0.5\left(\frac{-0.5}{100\varepsilon_{t,u}+0.3} + 0.005f_c' + 4.96\right) \quad (6)$$

where $f_{t,u}$ and f_c' are, respectively, the tensile and compressive strengths (MPa), and $\varepsilon_{t,u}$ is the tensile strain capacity (mm/mm). Employing Equation 4 to calculate MOR and taking $M_u = 0.5P_u a$, with P_u being the peak load (N) and a is the shear span (mm), the following empirical equation results:

$$f_{t,u} = \frac{6P_u a}{\left(\frac{-0.5}{100\varepsilon_{t,u}+0.3}+0.005f_c'+4.96\right)bh^2} \quad (7)$$

Accepted manuscript doi:
10.1680/jmacr.17.00199

which gives tensile strength in MPa. When the tensile strain capacity is larger than 1.5%, this equation can be further simplified whilst maintaining reasonable accuracy as the following:

$$f_{t,u} = \frac{3P_u a}{2.5bh^2} \tag{8}$$

where P_u is the peak load (N), a is the shear span (mm), b is the width of test specimen (=150 mm) and h is the overall depth (mm). To determine the tensile strength of ECC ($f_{t,u}$) during a quality control check, one would need to determine the applied load experimentally and then use Figure 8(b) or either Equation 7 or 8. Equation 7 should be used for tensile strain capacity values greater than 0.4% due to steep increase of the stress ratio at small strain values, whereas Equation 8 for strain values greater than 1.5%.

5.2 Predictions based on sectional analysis

To offer an alternative to the procedure described in Section 5.1, a calculation framework based on a sectional analysis approach is presented. From the strain diagram presented earlier in Figure 1(c), the beam curvature can be defined as:

$$\phi = \frac{\varepsilon_{t,u}}{h - x_c} = \frac{\varepsilon_{t,cr}}{y} \tag{9}$$

Employing the relations between beam curvature and beam deflection presented in Figures 9(a) and (b), which were obtained from the previous parametric analysis, and rearranging the first two terms of Equation 9 allow the value for the neutral axis depth, x_c (mm), to be determined:

$$x_c = \begin{cases} h - \frac{\varepsilon_{tu}}{6\times10^{-5}\delta_{u,m}} \\ h - \frac{\varepsilon_{tu}}{7.3\times10^{-5}\delta_{u,l}} \end{cases} \tag{10}$$

with h, $\delta_{u,m}$ and $\delta_{u,p}$ all in mm. Rearranging the last two terms of Equation 9 for y (in mm) gives the distance between the neutral axis and the location where first cracking occurs:

Accepted manuscript doi:
10.1680/jmacr.17.00199

$$y = \frac{\varepsilon_{t,cr}}{\varepsilon_{t,u}}(h - x_c) = \frac{\alpha f_{t,u}}{E_e \varepsilon_{t,u}}(h - x_c) \quad (11)$$

Assuming a bilinear stress-strain distribution, the resultant tensile force under the neutral axis, F_t (N), is:

$$F_t = \left(\left[0.5\frac{\alpha^2(h-x_c)}{E_e\varepsilon_{t,u}} - \left(\frac{\alpha+1}{2}\right)\frac{\alpha}{E_e\varepsilon_{t,u}}(h - x_c)\right] f_{t,u}^2 + \left[\left(\frac{\alpha+1}{2}\right)(h - x_c)\right] f_{t,u}\right) bh \quad (12a)$$

with E_e and $f_{t,u}$ in MPa, and h, x_c, b and h, in mm. The internal sectional moment around the neutral axis can be computed by multiplying Equation 12(a) with the lever arm, z (mm) (see Figure 9(c)), which can be approximated as

$$z = \left(-0.4\varepsilon_{t,u} + 0.547\right)h \quad (12b)$$

with $\varepsilon_{t,u}$ in (mm/mm) and h in mm. Equations 12(a) and (b) can be solved for $f_{t,u}$ by taking equilibrium of moment around the neutral axis. Solving these equations would be quite tedious if done by hand, but this can be done quite straightforward with a simple app or a dedicated online calculator (see, for instance, Suryanto *et al.*, 2017).

To provide a clear picture of the range of applicability of the proposed equations, FAsT was used to provide reference load-deflection values which were then inputted to Equations 7, 8 and 12. The results for specimens with a thickness of 50 mm and 75 mm are presented in Figure 10(a). It is evident that Equation 7 is the most superior despite its relative complexity. Equation 8, as expected, is less accurate, although it provides reasonably accurate estimates (within ±5% accuracy) for tensile strain capacity larger than 1.5%. Equation 12, which is the most flexible but the most onerous to solve, displays reasonably accurate estimates for tensile strain values larger than 0.8%. To obtain results with almost the same accuracy as the full analysis using the spreadsheet, Equations 7, 8 and 12 should only be used for tensile strain capacity greater than 0.4%, 1.5% and 0.8%, respectively.

Accepted manuscript doi:
10.1680/jmacr.17.00199

To demonstrate the use of the equations, Figure 10(b) compares the predicted stress-strain relationships for the 50-mm and 75-mm thick beam specimens to the envelope of the tensile stress-strain relationship obtained from the dog-bone tests reported by Paegle *et al.* (2016). The following average peak load and the corresponding average deflection were assumed: $\delta_{u,m} \cong 4.5$ mm and $P_u \cong 7.5$ kN for 50 mm thick specimen; and $\delta_{u,m} \cong 3.6$ mm and $P_u \cong 17.5$ kN for 75 mm thick specimen. When applied to each specimen thickness, it is apparent that whilst all the three equations provide conservative estimates of tensile strain capacities and strengths, they have very similar shapes and follow the trend of the experimental data reasonably well, with all curves being superimposed on each other. The discrepancy between the predictions and experimental data may come from the differences in fibre orientation which warrant further investigation.

6. Conclusions

The following conclusions can be drawn from the work presented:

1. The sectional analysis procedure presented in this paper is shown to be capable of predicting the flexural response of ECC beam specimens subjected to four-point bending, including the load-deflection, moment-curvature, longitudinal stress distributions, longitudinal curvature and deflection profiles. The procedure is implemented in Excel with a user-friendly interface, allowing users to input data and view analysis results with ease. The use of this spreadsheet is expected to add to the users understanding of the flexural behaviour of ECC. Further work is directed toward extending the calculation procedure via a webpage to allow public access.
2. Choosing an appropriate tensile stress-strain profile is shown to be essential to achieve the necessary level of accuracy with regards to the predictions of load and

deflection capacities. From the analysis of three series of available test data, it is shown that the bilinear tensile stress-strain model allows for more accurate results to be obtained, as well as facilitating the calculation of stress and strain at first cracking.

3. It is shown that due to flexural cracking, the curvature distribution over the shear span varies nonlinearly from the support and affects the predictions of deflection and tensile strain capacities.
4. The tensile strain capacity can be determined either from point- or mid-point beam deflection at the peak strength, provided that the two have a linear relationship over a narrow band of values. While the measurement of point-load deflection is simpler (viz, through readings from a testing machine), appropriate measures must be taken to avoid additional deflection resulting from bedding error and rig deformation being recorded thereby leading to inaccuracies.
5. Three empirical equations (Equations 7, 8 and 12) of different degree of complexity and accuracy are proposed to determine the tensile strength of ECC tested under four-point bending in accordance with the modified ASTM 1609 (ASTM, 2012), as recommended by Paegle *et. al* (2016). Equations 7, 8 and 12 should only be used for tensile strain capacity greater than 0.4%, 1.5% and 0.8%, respectively. The equations are relatively simple to use and, as such, are recommended for use in regular and frequent testing.
6.

Acknowledgements

The Authors gratefully acknowledge the financial supports of the School of Energy, Geoscience, Infrastructure and Environment at Heriot-Watt University.

Notation

a shear span

b width of beam specimen

c centre span

d thickness of individual layer on a cross section of beam specimen

E_o initial stiffness under uniaxial compression

E_e initial stiffness under uniaxial tension

E_{sh} stiffness during strain-hardening

f_c' compressive strength

$f_{t,cr}$ tensile cracking stress

$f_{t,u}$ tensile strength

h overall depth of beam specimen

K_o fracture parameter

n total number of layer

P applied load

P_u applied load at the peak

x_c neutral axis relative to the top face of beam specimen

y distance between the neutral axis and the tip of flexural crack

y_i positions of the centroid of layer i

z lever arm

α ratio of tensile cracking stress to tensile strength

β strain-rate factor

ε_c' strain at the peak compressive strength

ε_i longitudinal strain at the centroid of individual layer

ε_p plastic strain under uniaxial compression

$\varepsilon_{t,cr}$ strain corresponding to first cracking (taken as $\frac{f_{t,u}}{E_e}$)

$\varepsilon_{t,b}$ tensile strain at the centroid of the utmost bottom layer

$\varepsilon_{t,u}$ tensile strain capacity

$\delta_{u,m}$ mid-point deflection at peak strength

$\delta_{u,l}$ load-point deflection at peak strength

ϕ beam curvature

γ scale factor for strain calculations

ω_c compressive strength reduction factor due to transverse cracking

ω_t tensile strength reduction factor due to transverse cracking

References

Alyousif A, Anil O, Sahmaran M, Lachemi M, Yildirim G and Ashour AF (2015) Comparison of shear behaviour of engineered cementitious composite and normal concrete beams with different shear span lengths. *Magazine of Concrete Research* **68(5)**: 217–228.

ASTM (2012) ASTM C1609/C1609M-12: Standard test method for flexural performance of fiber reinforced concrete (using beam with third-point loading). ASTM International, West Conshohocken, PA, USA.

Fukuyama H and Suwada H (2003) Experimental response of HPFRCC dampers for structural control. *Journal of Advanced Concrete Technology* **1(3)**: 317–326.

Hou, LJ, Xu SL and Zhang XF (2012) Toughness evaluation of ultra-high toughness cementitious composite specimens with different depths. *Magazine of Concrete Research* **64(12)**: 1079–1088.

Huang X, Ranade R, Nia W and Li VC (2013) Development of green engineered cementitious composites using iron ore tailings as aggregates. *Construction and Building Materials* **44**: 757–764.

JCI (Japan Concrete Institute) (1984) JCI-SF4: Method of tests for flexural strength and flexural toughness of fiber reinforced concrete. JCI, Tokyo, Japan, pp. 45–51.

JCI-DFRCC Committee (2003) DFRCC terminology and application concepts. *Journal of Advanced Concrete Technology* **1(3)**: 335–340.

JCI (Japan Concrete Institute) (2007) JCI-S-003-2007: Method of test for bending moment–curvature of fiber reinforced cementitious composite. JCI, Tokyo, Japan.

Jun P and Mechtcherine V (2010). Behaviour of strain-hardening cement-based composites (SHCC) under monotonic and cyclic tensile loading: Part 1–Experimental investigations. *Cement and Concrete Composites* **32(10)**: 801–809.

Kanakubo T (2006) Tensile characteristics evaluation method for ductile fiber-reinforced cementitious composites. *Journal of Advanced Concrete Technology* **4(1)**: 3–17.

Kanda T, Saito T, Sakata N and Hiraishi M (2003) Tensile and anti-spalling properties of direct sprayed ECC. *Journal of Advanced Concrete Technology* **1(3)**: 269–282.

Kanda T, Tomoe S, Nagai S, Maruta M, Kanakubo T and Shimizu K (2006) Full scale processing investigation for ECC pre-cast structural element. *Journal of Asian Architecture and Building Engineering* **5(2)**: 333–340.

Kobayashi K, Anh DL and Rokugo K (2016) Effects of crack properties and water-cement ratio on the chloride proofing performance of cracked SHCC suffering from chloride attack. *Cement and Concrete Composites* **69**: 18–27.

Li VC (2008) Engineered Cementitious Composites (ECC) – Material, Structural, and Durability Performance. In *Concrete Construction Engineering Handbook* (Nawy EG (ed)). CRC Press, Boca Raton, United States of America, pp. 24-1–24-46.

Li VC and Stang H (2004) Elevating FRC material ductility to infrastructure durability. In *Proceedings of the International RILEM Symposium on Fiber Reinforced Concrete – BEFIB 2004* (di Prisco M, Felicetti R and Plizzari GA (eds)). RILEM Publications, Varenna, Italy, pp. 171–186.

Maalej M and Li VC (1994) Flexural/tensile strength ratio in engineered cementitious composites. *Journal of Materials in Civil Engineering* **ASCE 6(4)**: 513–28.

Maekawa K, Okamura H and Pimanmas A (2003) Nonlinear mechanics of reinforced concrete. Spon press, London, UK, Chapter 2.

Matsumoto T, Wangsiripaisal K, Hayashikawa T and He X (2010) Uniaxial tension-compression fatigue behavior and fiber bridging degradation of strain hardening fiber reinforced cementitious composites. *International Journal of Fatigue* **32(11)**: 1812–1822.

Mechtcherine V (2012) Towards a durability framework for structural elements and structures made of or strengthened with high-performance fibre-reinforced composites. *Construction and Building Materials* **31**: 94–104.

Paegle I, Minelli F and Fischer G (2016) Cracking and load-deformation behavior of fiber reinforced concrete: influence of testing method. *Cement and Concrete Composites* **73**: 147–163.

Qian S and Li VC (2007) Simplified inverse method for determining the tensile strain capacity of strain hardening cementitious composites. *Journal of Advanced Concrete Technology* **5(2)**: 235–246.

Qian S and Li VC (2008) Simplified inverse method for determining the tensile strain properties of strain hardening cementitious composites (SHCC). *Journal of Advanced Concrete Technology* **6(2)**: 353–363.

Shin KJ, Jang KH, Choi YC and Lee SC (2015) Flexural behavior of HPFRCC members with inhomogeneous material properties. *Materials* **8(4)**: 1934–1950.

Siad H, Lachemi M, Sahmaran M, Mesbah HA, Anwar Hossain KM and Ozsunar A (2017) Potential for using recycled glass sand in engineered cementitious composites. *Magazine of Concrete Research* **69(17)**: 905–918.

Sisomphon K, Copuroglu O and Koenders EAB (2013) Effect of exposure conditions on self healing behavior of strain hardening cementitious composites incorporating various cementitious materials. *Construction and Building Materials* **42**: 217–224.

Soranakom C and Mobasher B (2008) Correlation of tensile and flexural responses of strain softening and strain hardening cement composites. *Cement and Concrete Composites* **30(6)**: 465–477.

Suryanto B, Nagai K and Maekawa K (2010a) Bidirectional multiple cracking tests on high-performance fiber-reinforced cementitious composite plates. *ACI Material Journal* **107(5)**: 450–460.

Suryanto B, Nagai K and Maekawa K (2010b) Modeling and analysis of shear-critical ECC members with anisotropic stress and strain fields. *Journal of Advanced Concrete Technology* **8(2)**: 239–258.

Suryanto B, Nagai K and Maekawa K (2010c) Smeared-crack modeling of R/ECC membranes incorporating an explicit shear transfer model. *Journal of Advanced Concrete Technology* **8(3)**: 315–326.

Suryanto B, Wilson SA, McCarter WJ and Chrisp TM (2016) Self-healing performance of engineered cementitious composites under natural environmental exposure. *Advances in Cement Research* **28(4)**: 211–220.

Suryanto B, Cockburn B, Han AL and McCarter WJ (2017) An alternative method for determining tensile properties of engineering cementitious composites. *Procedia Engineering* **171**: 584–591.

Suryanto B, McCarter WJ, Starrs G and Ludford-Jones GV (2016) Electrochemical immittance spectroscopy applied to a hybrid PVA/steel fiber engineered cementitious composite. *Material and Design* **105**: 179–189.

van Zijl G.P.A.G., Slowik V, Toledo Filho RD, Wittmann FH and Mihashi H (2015) Comparative testing of crack formation in strain-hardening cement-based composites (SHCC). *Materials and Structures* **49(4)**: 1175–1189.

Wang S and Li VC (2007) Engineered cementitious composite with high-volume fly ash. *ACI Material Journal* **104(3)**: 233–241.

Yun HD, Yang IS, Kim SW, Jeon E, Choi CS and Fukuyama H (2007) Mechanical properties of high-performance hybrid-fibre-reinforced cementitious composites (HPHFRCCs). *Magazine of Concrete Research* **59(4)**:257–271.

Zhou J, Qian S, Beltran MGS, Ye G, van Breugel K and Li VC (2010) Development of engineered cementitious composites with limestone powder and blast furnace slag. *Materials and Structures* **43(6)**: 803–814.

Accepted manuscript doi:
10.1680/jmacr.17.00199

Figure 1. (a) Schematic of an ECC beam tested under four-point bending; (b) structural model representation of half of the beam; and (c) discretization of beam cross-section into layers and the corresponding strain and stress profiles across the depth.

Figure 2. Constitutive models employed in the calculation.

Figure 3. Algorithm for beam analysis.

Figure 4. (a) Calculation procedure and screenshots of main terminal displaying (b) the entry (white) boxes for user input; and (c) the output.

Figure 5. (a) Comparison of the observed and assumed tensile stress-strain models for Maalej and Li' specimens, with the experimental data representing the envelope of the reported data; (b) predicted and observed equivalent flexural stress vs deflection responses; (c) and (d) predicted curvature profiles based on the bilinear and elastic-plastic models. The inset in (d) representing an enlarged image of the curvature profile obtained from the first three load steps.

Figure 6. (a) Comparison of observed and assumed tensile properties; (b) predicted and observed moment-curvature at the critical section for Kanakubo beam specimens (Kanakubo, 2006), with the experimental data representing the envelope of test data reported in the original paper; (c) predicted longitudinal stress distributions; and (d) predicted equivalent flexural stress vs mid-point deflection for the two tensile models.

Figure 7. (a) Comparison of observed and assumed tensile properties for Paegle specimens (Paegle *et al.*, 2016); (b) to (d) comparison of predicted and observed load-deflection for specimens with a thickness of 50, 75 and 150 mm, respectively. The experimental data represent the envelope of the reported test data.

Figure 8. (a) Predicted deflection at peak load plotted against tensile strain capacity; and (b) ratio of equivalent flexural strength to tensile strength plotted against tensile strain capacity.

Figure 9. The relation between beam curvature and beam deflection at peak load for (a) 50 mm- and (b) 75 mm-thick specimens; and (c) normalised lever arm plotted against tensile strain capacity for both specimen thicknesses.

Figure 10. (a) The accuracy of the proposed equations in determining tensile strength. The material parameters used in the parametric analysis were: E_s = 18 GPa; α = 0.8; f_c' = 40, 50 and 60 MPa; f_{tu} = 3.5, 4 and 5 MPa; (b) predicted stress-strain profiles plotted against dog-bone test results.

Accepted manuscript doi:
10.1680/jmacr.17.00199

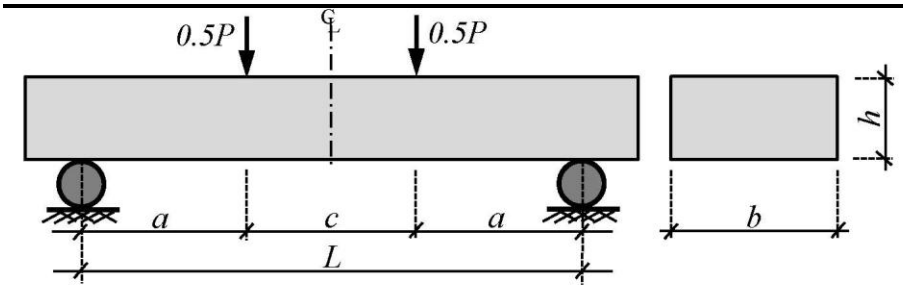

(a)

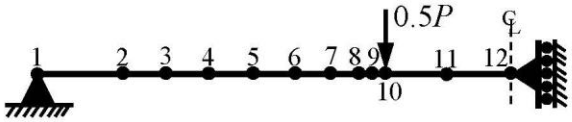

(b)

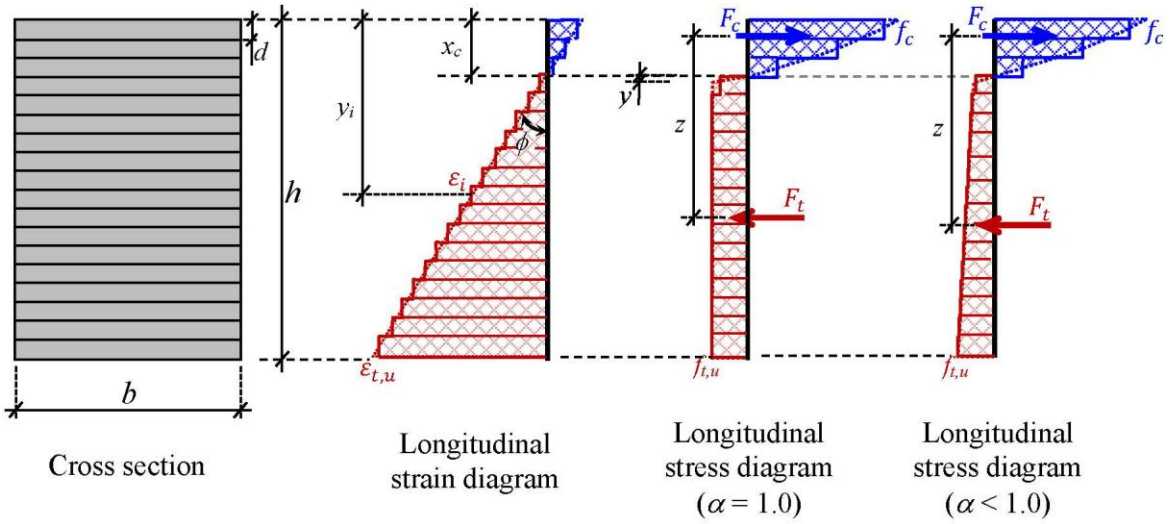

(c)

Figure 1.

Accepted manuscript doi:
10.1680/jmacr.17.00199

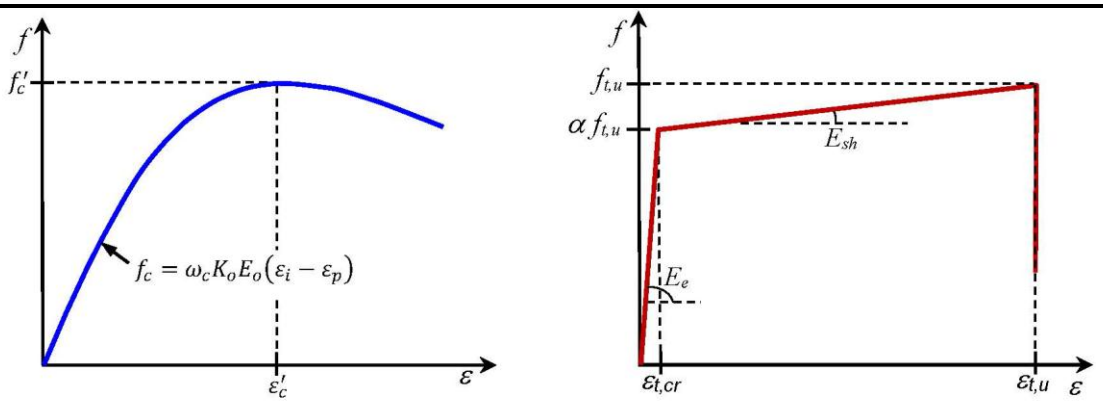

Figure 2.

Accepted manuscript doi:
10.1680/jmacr.17.00199

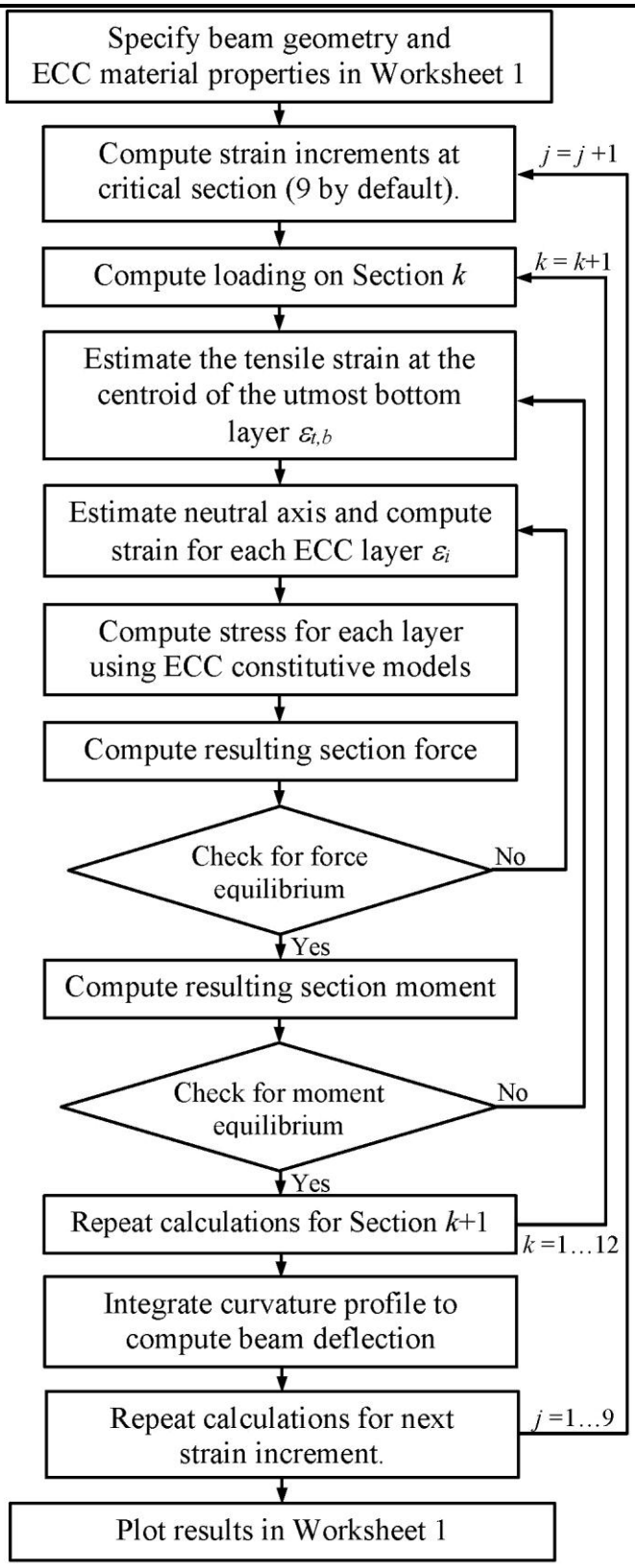

Figure 3.

Accepted manuscript doi:
10.1680/jmacr.17.00199

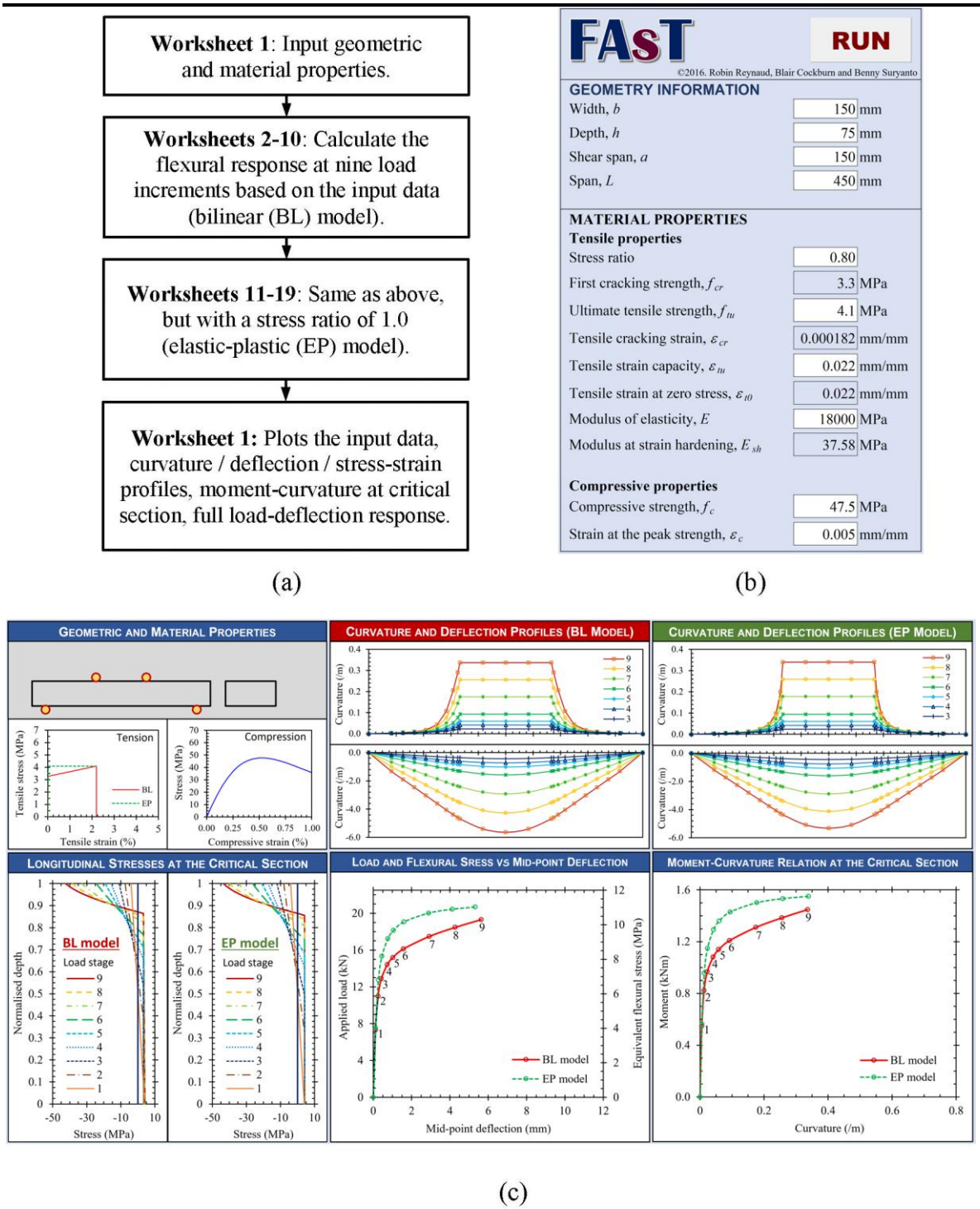

Figure 4.

Accepted manuscript doi:
10.1680/jmacr.17.00199

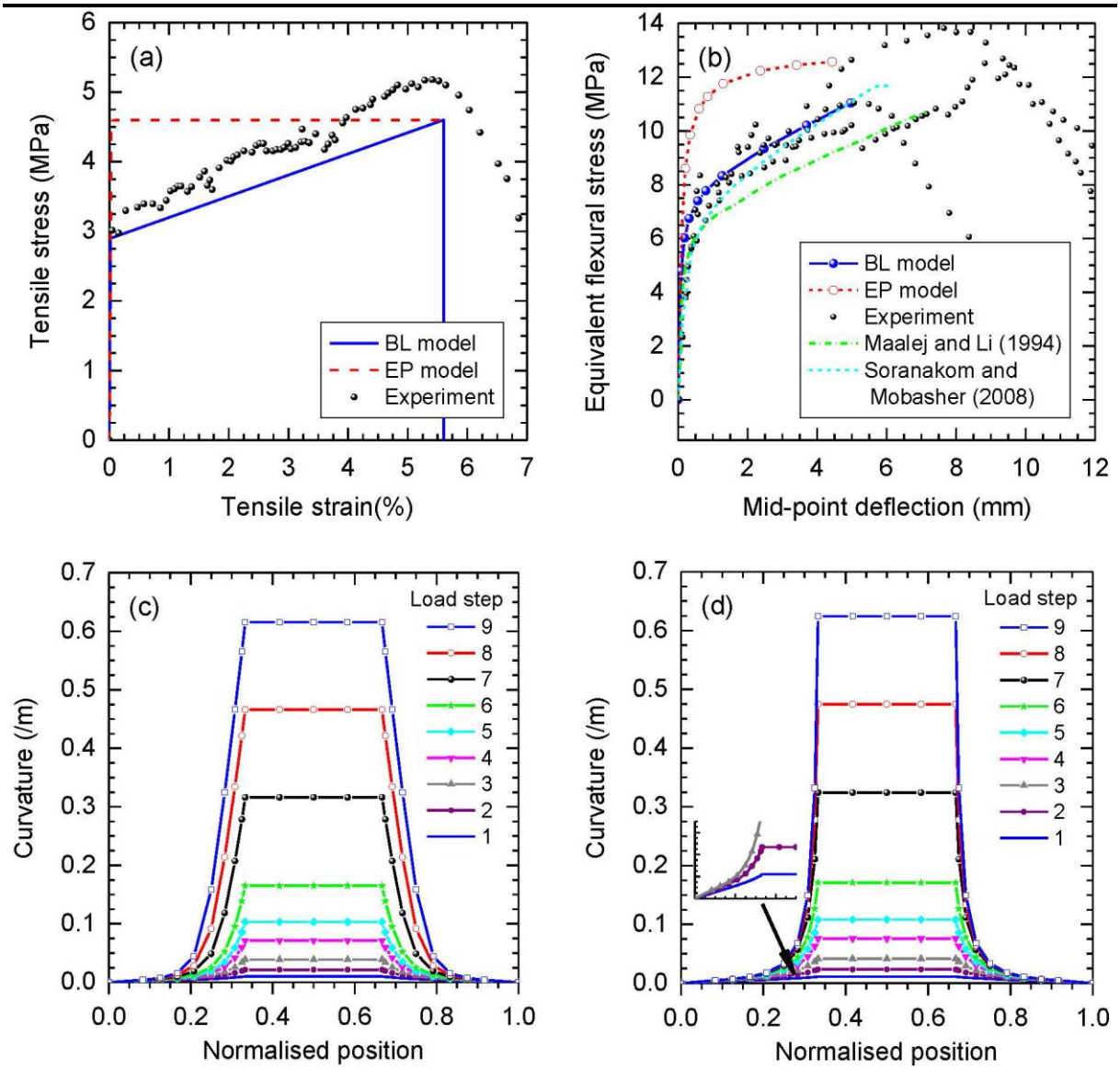

Figure 5.

Accepted manuscript doi:
10.1680/jmacr.17.00199

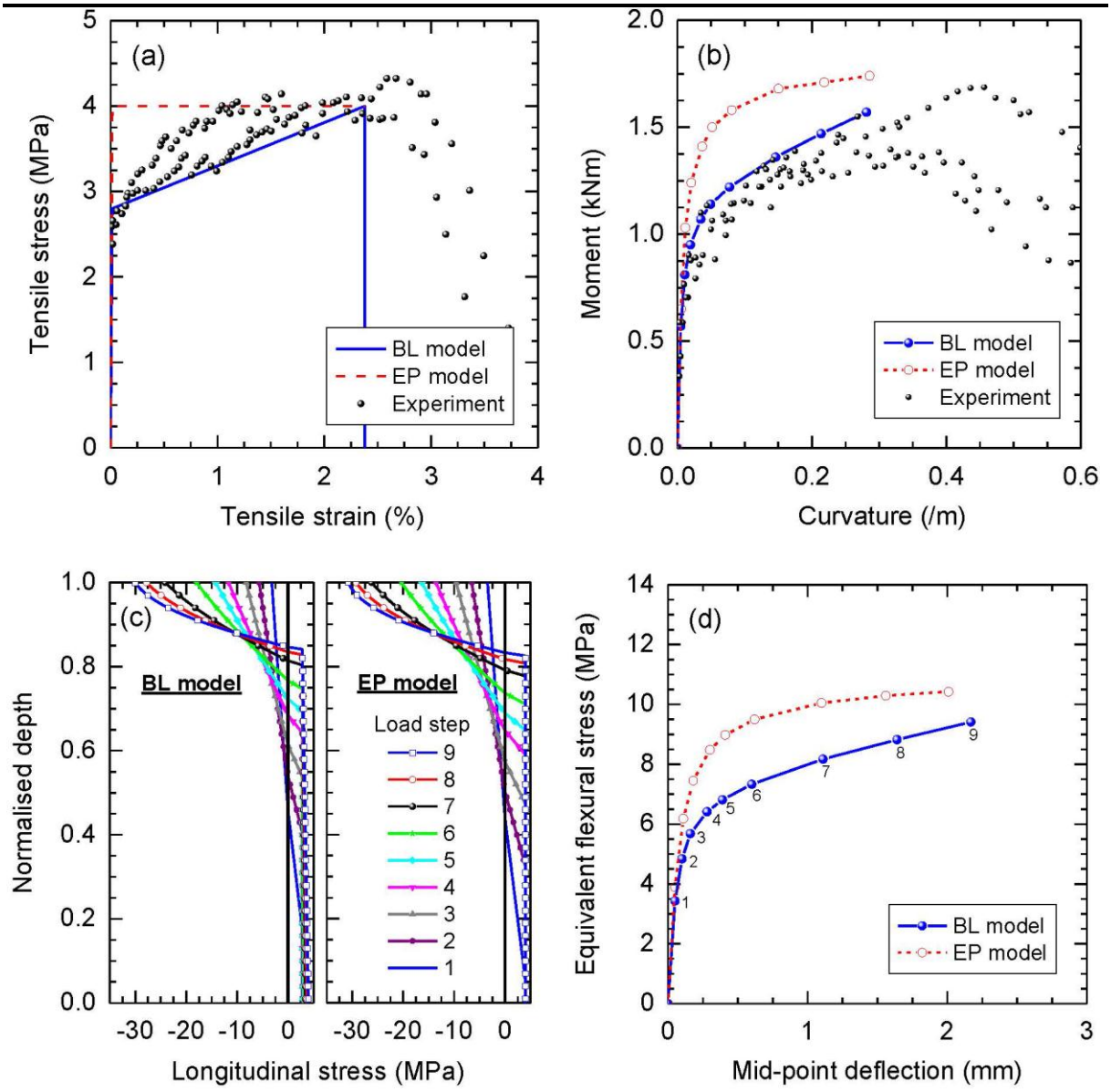

Figure 6.

Accepted manuscript doi:
10.1680/jmacr.17.00199

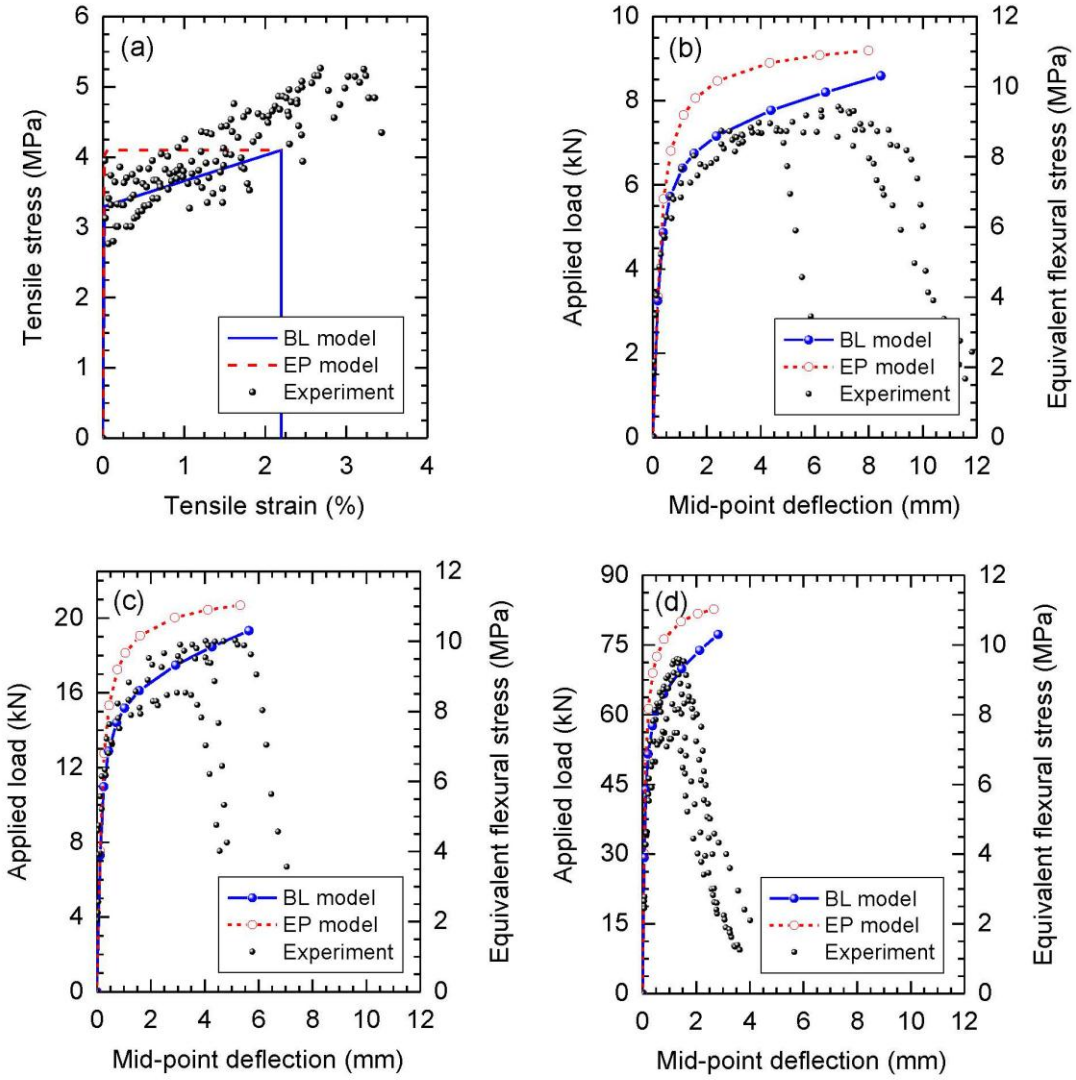

Figure 7.

Accepted manuscript doi:
10.1680/jmacr.17.00199

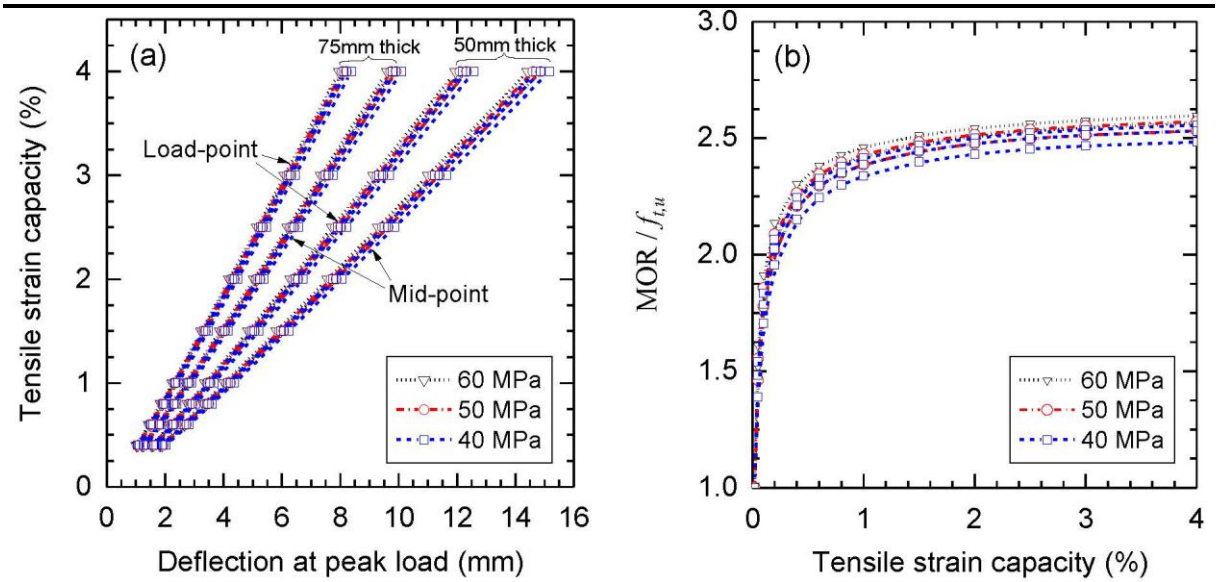

Figure 8.

Accepted manuscript doi:
10.1680/jmacr.17.00199

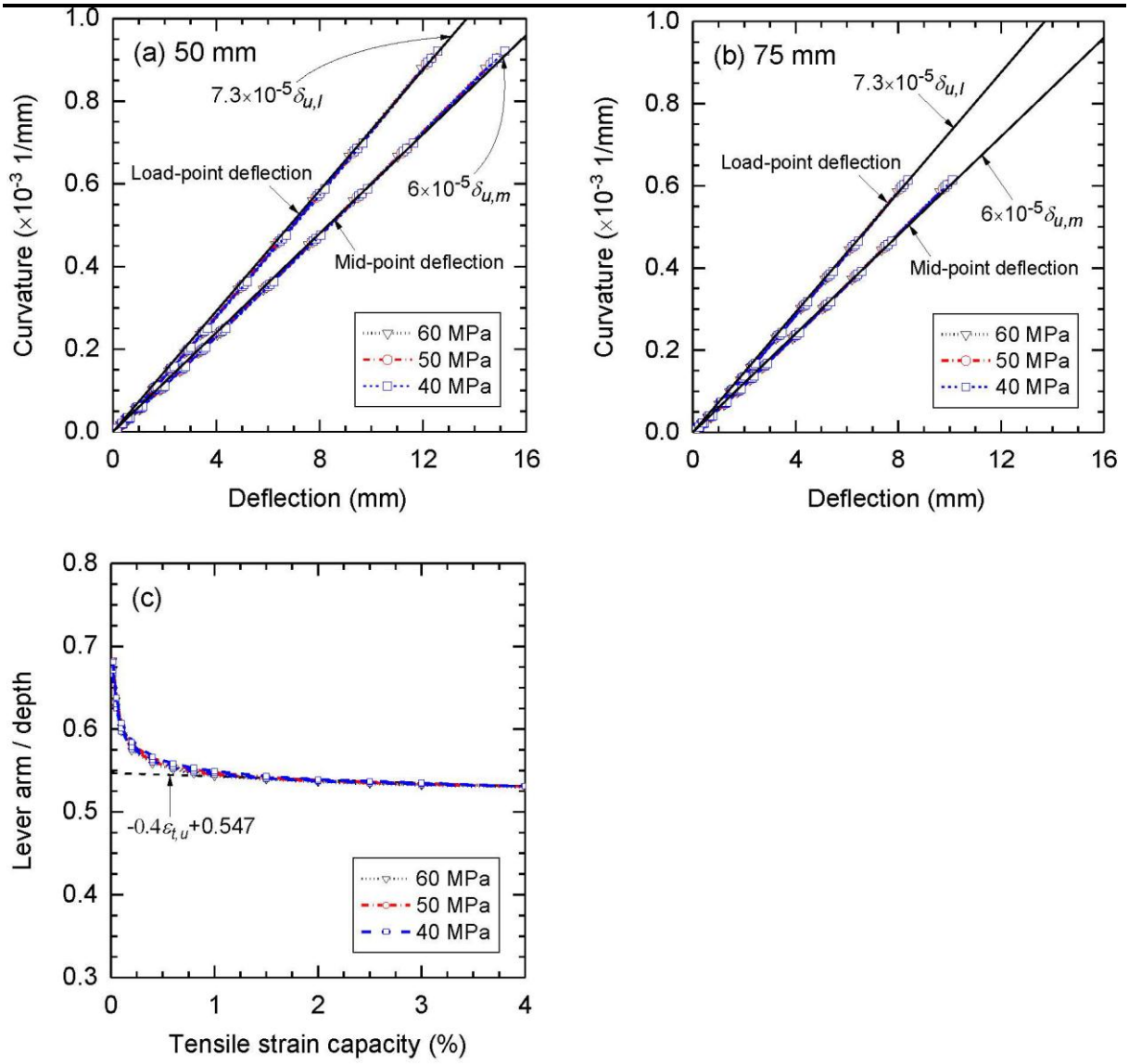

Figure 9.

Accepted manuscript doi:
10.1680/jmacr.17.00199

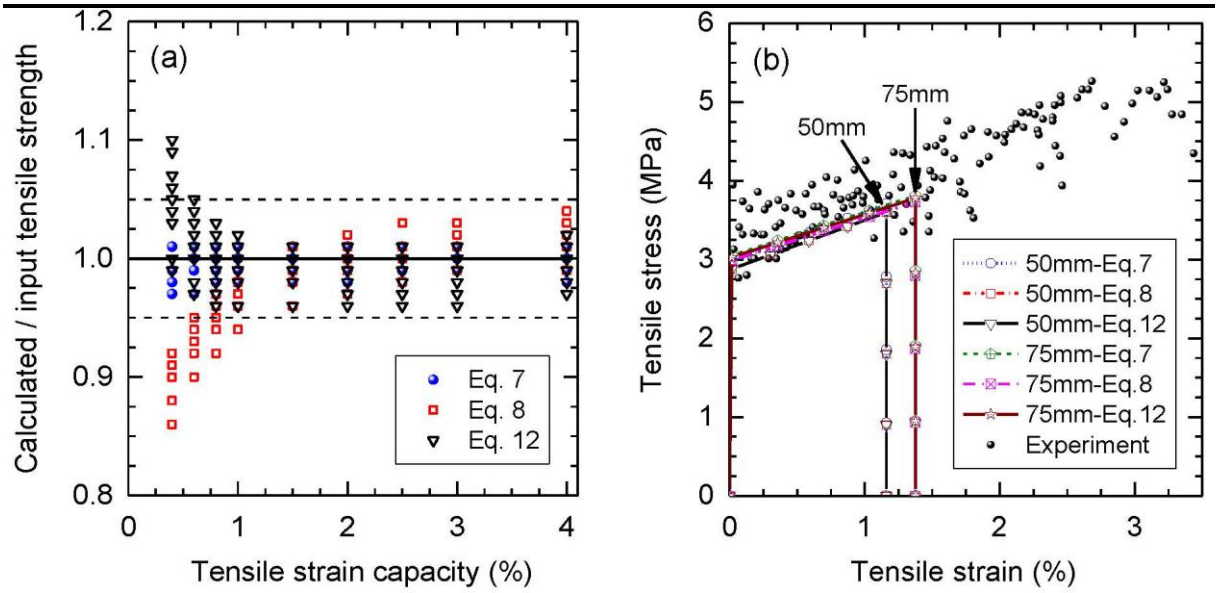

Figure 10.